Hang Xu
Department of Mechanical Engineering,
McGill University,
817 Sherbrooke Street West,
Montreal, QC, H3A 0C3, Canada
e-mail: hang.xu@mail.mcgill.ca

Amr Farag
Department of Mechanical Engineering,
McGill University,
817 Sherbrooke Street West,
Montreal, QC, H3A 0C3, Canada
e-mail: amr.farag@mail.mcgill.ca

Ruizhe Ma
Department of Mechanical Engineering,
McGill University,
817 Sherbrooke Street West,
Montreal, QC, H3A 0C3, Canada
e-mail: ruizhe.ma@mail.mcgill.ca

Damiano Pasini[1]
Mem. ASME
Department of Mechanical Engineering,
McGill University,
817 Sherbrooke Street West,
Montreal, QC, H3A 0C3, Canada
e-mail: damiano.pasini@mcgill.ca

Thermally Actuated Hierarchical Lattices With Large Linear and Rotational Expansion

This paper presents thermally actuated hierarchical metamaterials with large linear and rotational motion made of passive solids. Their working principle relies on the definition of a triangular bi-material unit that uses temperature changes to locally generate in its internal members distinct rates of expansion that translate into anisotropic motions at the unit level and large deployment at the global scale. Obtained from solid mechanics theory, thermal experiments on fabricated proof-of-concepts and numerical analysis, the results show that introducing recursive patterns of just two orders of the hierarchy is highly effective in amplifying linear actuation at levels of nearly nine times the initial height, and rotational actuation of almost 18.5 times the initial skew angle.
[DOI: 10.1115/1.4044026]

1 Introduction

Temperature-responsive and -tunable materials are in high demand for a broad range of applications across disciplines, including morphable structures [1–3], deployable systems [4,5], drug delivery devices [6], MEMS [7], and actuators [8], among others. In the realm of architected materials responsive to temperature, concepts with tunable thermal expansion have been engineered from either active or passive solids, or a combination thereof, to deliver large positive, or negative, value of thermal expansion [9,10]. Among those made of passive solids, typical concepts consist of two materials with a distinct coefficient of thermal expansion (CTE) that are topologically arranged and geometrically tailored to attain desired thermal responses [11,12]. Among those that are stretch-dominated with high specific stiffness, there are concepts capable of offering zero, negative, and positive (even unbounded [13]) CTE, but their thermal response is mainly linear isotropic, with a magnitude of deformation spanning a limited range [14–16]. On the other hand, concepts that are bend-dominated can attain other than linear expansion and isotropic CTE, and they can do so by accommodating thermal strain mismatches in their architecture, a deformation mechanism that generates specific changes, such as variation of angle either in-plane, e.g., included angle of curved beam [17], or spatially, e.g., opening angle in Origami [3]; however, their structural efficiency is low. From the distinct characteristics of these two groups, we gather that stiff and lightweight architectures capable of generating anisotropic and large actuation responses have not been explored yet. However, this is not uncommon in the domain of conventional materials. A degree of CTE anisotropy, for example, can be found in stiff solids [18,19]; yet, the deformation amplitude they can offer is orders of magnitude

smaller than the scale of deformation that is sought in certain applications requiring large actuation, such as deployable structures [20–22], in specific directions.

The goal of this work is twofold. The first is to present stretch-dominated material concepts made of passive solids that can be thermally actuated to generate not only linear but also rotational deformation, hence contributing to access anisotropic thermal responses. The second is to achieve extremely large-scale thermal expansion with actuation values comparable with, or well above, those of typical actuators, such as strains as high as 100% for a temperature change of 70 °C [8]. The paper starts with a description of a planar stiff and lightweight unit with pin-jointed elements that can offer both linear and rotational thermal deformation. Then, structural hierarchy is pursued in pin-jointed lattices to amplify their global actuation response. Proofs-of-concept are built and tested to validate closed-form expressions derived from mechanics theory and further verified through numerical analysis. A discussion closes the paper and compares the performance of the class of architected materials here presented with other materials used as actuators.

2 Thermal Expansion of Dual-Material Triangular Sub-Cell

The focus of this section is to first describe a bi-material lightweight concept with a stretch-dominated pin-jointed topology that upon a change in temperature can generate multiple types of deformation, including linear and rotational. The following introduces the geometry of a sub-cell, provides closed-form expressions for its thermal expansion, and analyses the role of its material and geometric constituents.

2.1 Sub-Cell Geometry. Figure 1(*a*) illustrates a triangular sub-cell with two pin-jointed solids of distinct CTE, capable of attaining both linear and rotational thermal expansion. Upon a uniform change in temperature, the solid (inclined sides) with high CTE α_{s1} and its counterpart (base) with low CTE α_{s2} deform
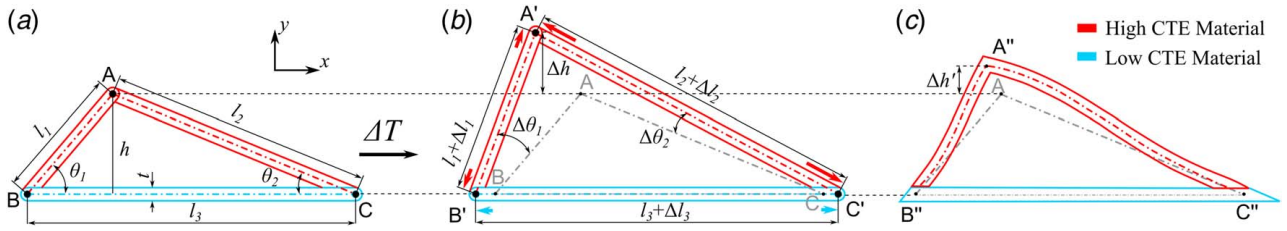

Fig. 1 (*a*) Bi-material triangle sub-cell with strut thickness *t*, sloped bar lengths l_1 and l_2 (high-CTE material), horizontal bar length l_3 (low-CTE material), and skew angles θ_1 and θ_2. Deformed state of the pin-jointed (*b*) and rigid-jointed (*c*) sub-cell with qualitative dimensional changes under a representative temperature change of ΔT. (Color version online.)

at different rates, with the high-CTE members generating an overall height, as well as slight width, increase. While the position of the constituent bars could be swapped, the choice of assigning the high CTE material to the skewed members, as opposed to other possible cases, is here motivated by the intent of creating a high CTE concept that maximizes the thermal expansion in the *y*-direction [13].

For the lattice concepts presented here, the mechanism of temperature-induced deformation that enables a change in the internal angles ($\Delta\theta_1$ and $\Delta\theta_2$) and the height (Δh) is the mismatched deformation of the struts expanding at their own rate. This is shown in Fig. 1(*b*), where the deformed state of the sub-cell is visualized in its pin-jointed version with struts rotating freely at their nodes.

Figure 1(*c*) shows its rigid-jointed counterpart, where the restricted rotation at the nodes creates a degree of bending in the struts, thus generating a height change Δh that is lower than that of the pin-jointed concept. By harnessing, the values of α_{s1} and α_{s2} or the skewness of the inclined bars θ_1 and θ_2, we can tune Δh in the *y*-direction as well as the degree of additional rotation $\Delta\theta_1$ and $\Delta\theta_2$ of the angles θ_1 and θ_2, respectively. While both versions allow CTE tuning, a comparison between the two (Fig. 1(*b*) versus 1(*c*)) shows that the former deforms more than the latter, hence being preferred for actuation purposes.

The above description on the two modes of deformation accrued in a sub-cell under ΔT allows us to examine both a linear and rotational CTE (RCTE). The linear expression of CTE (LCTE) in the *y*-direction is simply given by

$$\alpha_{LCTE,y} = \frac{\Delta h}{h \cdot \Delta T} \tag{1}$$

where *h* is the representative height of the sub-cell at a reference temperature T_0, $\Delta T = T - T_0$ is the change of temperature, and Δh is the change in height.

Similarly, the change in the internal angle $\Delta\theta_1$ with respect to the initial inclination θ_1 allows to define the RCTE along θ_1 as

$$\alpha_{RCTE,\theta_1} = \frac{\Delta\theta_1}{\theta_1 \cdot \Delta T} \tag{2}$$

Since a simple switch of the subscripts in the expression above allows to write the RCTE in the direction of the angle θ_2, from now on we examine α_{RCTE,θ_1} only.

For the general case of a pin-jointed sub-cell (Fig. 1(*a*)) with arbitrary skew angles θ_1 and θ_2, there is no thermal stress caused by a temperature change. Hence, the thermal deformation magnitude of a sub-cell, i.e., the displacement in the *y*-direction (Δh) and relative rotation along θ_1 ($\Delta\theta_1$), can be evaluated via a geometric analysis of the beam element assembly prior and post thermal expansion such that

$$\Delta h = l_1 (1 + \alpha_{s1}\Delta T)$$
$$\left\{ 1 - \left[\frac{\xi^2 \sin(\theta_2 - \theta_1) + \sin(\theta_2 + \theta_1)}{2\xi \sin\theta_2} \right]^2 \right\}^{1/2} - l_1 \sin\theta_1 \tag{3}$$

$$\Delta\theta_1 = \arccos\left(\frac{\xi^2 \sin(\theta_2 - \theta_1) + \sin(\theta_2 + \theta_1)}{2\xi \sin\theta_2} \right) - \theta_1 \tag{4}$$

where l_1 is the initial length of the high-CTE element AB in Fig. 1(*a*) and $\xi = (1 + \alpha_{s1}\Delta T)/(1 + \alpha_{s2}\Delta T)$.

Substituting Eqs. (3) and (4) in Eqs. (1) and (2) yields, respectively, the LCTE in the *y*-direction and the RCTE of θ_1 as

$\alpha_{LCTE,y} =$

$$\frac{1 + \alpha_{s1}\Delta T}{\sin\theta_1\Delta T} \left\{ 1 - \left[\frac{\xi^2 \sin(\theta_2 - \theta_1) + \sin(\theta_2 + \theta_1)}{2\xi \sin\theta_2} \right]^2 \right\}^{1/2} - \frac{1}{\Delta T} \tag{5}$$

$$\alpha_{RCTE,\theta_1} = \left(\arccos\left(\frac{\xi^2 \sin(\theta_2 - \theta_1) + \sin(\theta_2 + \theta_1)}{2\xi \sin\theta_2} \right) - \theta_1 \right) \Big/ (\theta_1\Delta T) \tag{6}$$

From Eqs. (5) to (6), we gather that $\alpha_{LCTE,y}$ and α_{RCTE,θ_1} depend on two sets of sub-cell characteristics, i.e., the CTE of the constituent materials, α_{s1} and α_{s2}, and the skew angles, namely θ_1 and θ_2.

The following section examines the role that the sub-cell parameters, i.e., material properties (α_{s1} and α_{s2}) and geometric parameters (θ_1 and θ_2), play in the LCTE and RCTE of a sub-cell. The results provide a foundational basis for understanding sub-cell expansion as well as guidelines for the generation of compound units with large CTE.

2.2 Influence of Sub-Cell Parameters on Thermal Expansion

2.2.1 Coefficient of Thermal Expansion Role of Constituent Solids. From inspection of Eqs. (5) and (6), we gather that the thermal expansion of a sub-cell with given geometry is controlled by the absolute magnitude of the two constituent CTEs α_{s1} and α_{s2}, the two independent material parameters. To identify zones of the material space with high CTE, we plot in Fig. 2 their expressions as a function of one of the constituent CTEs and their proportion (i.e., $\lambda = \alpha_{s1}/\alpha_{s2}$). In Fig. 2(*a*), $\alpha_{LCTE,y}$ is visualized as a contour of α_{s2} versus λ, making straightforward to identification of the region (top right) with high LCTE. From this figure, we gain the following insights. Maximizing $\alpha_{LCTE,y}$ calls for a pair of materials with large CTE distinction, i.e., high λ, and a large CTE value of one of the material constituents, between which we chose here α_{s2}. Analogously for the effective RCTE, Fig. 2(*b*) reveals a similar trend, where the high α_{RCTE,θ_1} is obtained by large values of both the absolute magnitude of one (α_{s2}) of the CTE constituents and their CTE ratio (λ).

2.2.2 Role of Sub-Cell Geometric Parameters. Having examined the role of the material CTEs, we now focus on the sub-cell geometry, and for given constituent CTEs and $\Delta T = 100\,°\mathrm{C}$, we investigate the role of the main geometric parameters in the effective thermal deformation and effective CTE.
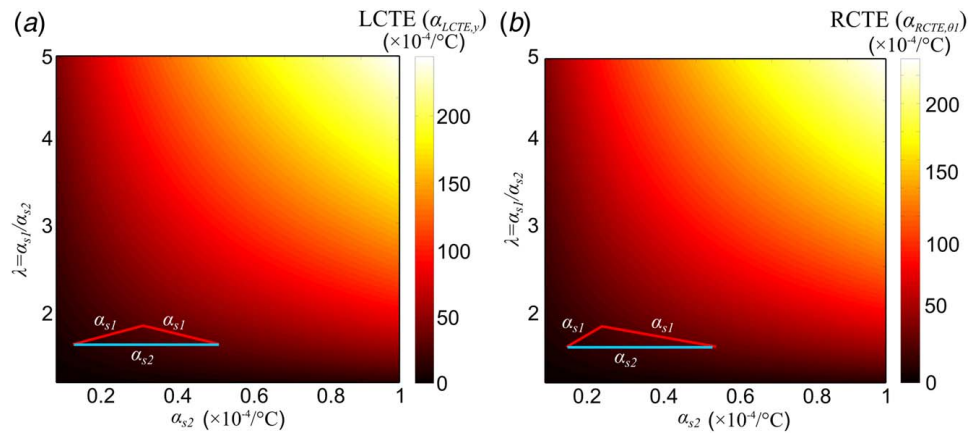
Fig. 2 Contour plots of LCTE and RCTE versus the absolute magnitude of the low-CTE constituent α_{s2} and the CTE proportion $\lambda = \alpha_{s1}/\alpha_{s2}$ for given sub-cell geometry (a) $\alpha_{LCTE,y}$ for sub-cell with $\theta_1 = \theta_2 = 5$ deg, and (b) α_{RCTE,θ_1} for sub-cell with $\theta_1 = 8$ deg and $\theta_2 = 2$ deg under $\Delta T = 100\,°C$. All coefficients are expressed in $10^{-4}/°C$ to express the actual expansion for a temperature change of 100 °C.
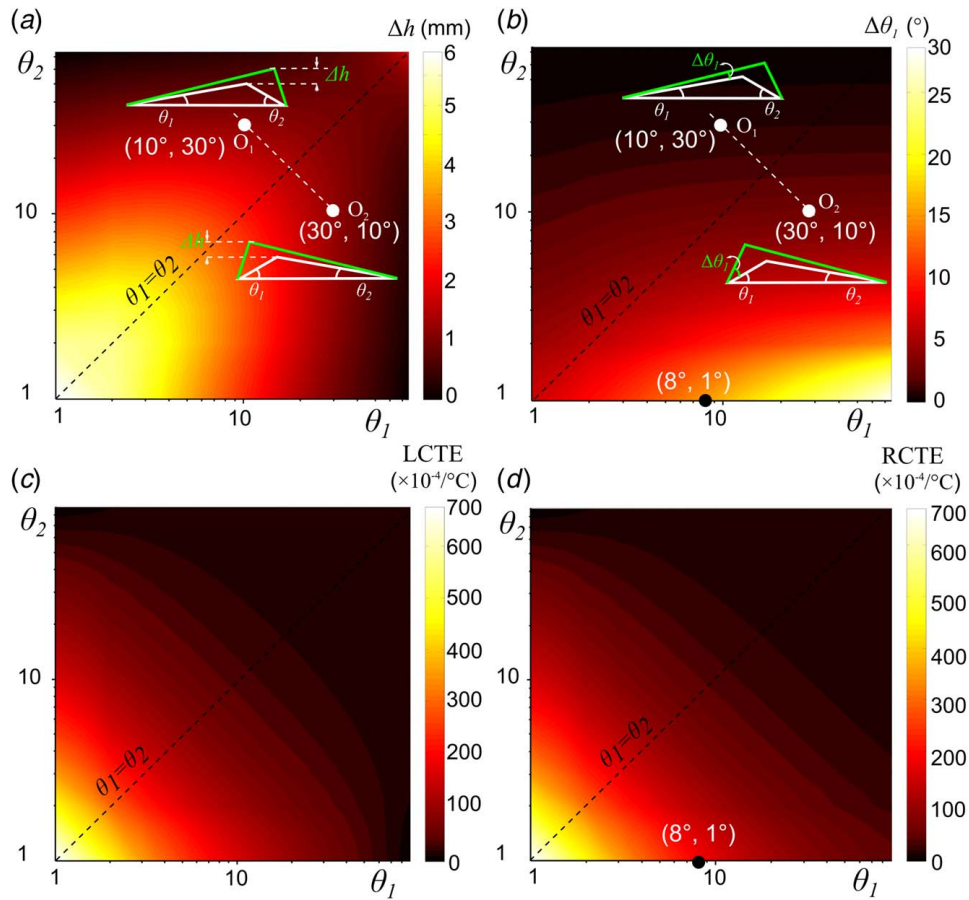

Fig. 3 Log-log contour plots for given $\Delta T = 100\,°C$, showing (a) height change Δh, (b) left skew angle variation $\Delta\theta_1$, (c) linear coefficient of thermal expansion (LCTE) in the y-direction, and (d) rotational coefficient of thermal expansion (RCTE) of the left skew angle (θ_1) versus θ_1 and θ_2, both in the representative range 1–89 deg shown in the log scale. Data obtained for given $l_3 = 100$ mm, $\alpha_{s1} = 100 \times 10^{-6}/°C$, and $\alpha_{s2} = 10 \times 10^{-6}/°C$

Figures $3(a)$ and $3(b)$ plot contours of the thermal deformation magnitude, i.e., Δh (Eq. (3)) and $\Delta\theta_1$ (Eq. (4)), versus the skew angles θ_1 and θ_2, and Figs. $3(c)$ and $3(d)$ show how the skew angles govern their LCTE (Eq. (5)) and RCTE (Eq. (6)). While Figs. $2(a)$ and $2(b)$ show that the constituent CTEs have a similar

impact on both their linear and rotational thermal expansion, Fig. 3 shows that varying θ_1 and θ_2 has an outcome that is specific to LCTE and RCTE. In particular, a symmetry of contours (Δh and $\alpha_{LCTE,y}$) with respect to the diagonal $\theta_1 = \theta_2$ appears in Figs. $3(a)$ and $3(c)$, as opposed to Figs. $3(b)$ and $3(d)$. This indicates that a

switch of the initial values for θ_1 and θ_2 (symmetric points O_1 and O_2 in Fig. 3(a)) has no effect on the height change (Δh) of the sub-cell. Besides contour symmetry, we observe the monotonic decrease of both Δh and LCTE with the increase of the skew angles. The smaller θ_1 and θ_2, i.e., a triangle with lower slopes, the larger LCTE. The initial configuration that would most maximizing both Δh and $\alpha_{LCTE,y}$ is the one with θ approaching 0, i.e., a closed sub-cell with sides almost resting on its base. These observations show that among sub-cell candidates satisfying a given geometric condition, such as $\theta_1 + \theta_2 = \text{const.}$ (see example of line $\theta_1 + \theta_2 = 40$ deg in Fig. 3(a)), those that maximize $\alpha_{LCTE,y}$ would have $\theta_1 = \theta_2$. This condition describes an isosceles triangle with maximum linear deformation and LCTE (L-sub-cell) that, respectively, reduce from Eqs. (3) and (5) to

$$\Delta h = l_1[(1 + \alpha_{s1}\Delta T)^2 - \cos^2\theta(1 + \alpha_{s2}\Delta T)^2]^{1/2} - l_1\sin\theta \quad (7)$$

$$\alpha_{LCTE,y} = \frac{\sqrt{(1 + \alpha_{s1}\Delta T)^2 - \cos^2\theta(1 + \alpha_{s2}\Delta T)^2}}{\Delta T\sin\theta} - \frac{1}{\Delta T} \quad (8)$$

In contrast to the symmetry of LCTE contours, Figs. 3(b) and 3(d) show asymmetry for both $\Delta\theta_1$ and α_{RCTE,θ_1} with respect to $\theta_1 = \theta_2$ throughout the range of $0 < \theta < 90$ deg. In this case, a swap of the initial values θ_1 and θ_2 (points O_1 and O_2) results in a dissimilar outcome. The change of the initial value of θ_1 leads to a variation in both $\Delta\theta_1$ ($\Delta\theta_1 = \Delta\theta_{1,\Delta T} - \theta_1$) and $\alpha_{RCTE,\theta_1}(\alpha_{RCTE,\theta_1} = \Delta\theta_1/(\theta_1 \cdot \Delta T))$, which depend on θ_1. Besides contour asymmetry, Fig. 3(b) shows the monotonic increase of $\Delta\theta_1$ with the increase of θ_1 and the decrease of θ_2 for a given ΔT. This indicates that maximizing $\Delta\theta_1$ would require a large relative difference between θ_1 and θ_2. On the other hand, Fig. 3(d) illustrates the need for shallow skew angles to generate large α_{RCTE,θ_1}. Therefore, while both $\Delta\theta_1$ and α_{RCTE,θ_1} are strongly governed by θ_1, the former has an inverse proportionality with θ_1, whereas the latter direct. Boosting $\Delta\theta_1$ requires a large distinction between the initial angles θ_1 and θ_2, whereas low values of their initial angles maximize α_{RCTE,θ_1}. This condition describes a scalene triangle.

While the insights gained from the above analysis apply to sub-cells with ideal geometry, we note that practical issues should be considered in the selection of the sub-cell parameters. This appears manifest in Sec. 3, where a representative set of rotational R-sub-cells with $\theta_1 \approx 8$ deg and $\theta_2 \approx 1$ deg is chosen to generate compound units capable of generating large RCTE.

3 Metamaterial Lattices With Linear and Rotational Coefficient of Thermal Expansion

Section 2 has shown that to achieve large $\alpha_{LCTE,y}$ for a given ΔT, the L-sub-cell should form an isosceles triangle that provides linear actuation. On the other hand, to maximize α_{RCTE,θ_1}, the R-sub-cell should resemble a skewed triangle featuring θ_1 and θ_2 in the low skew angles regime, hence providing high values of rotation. These insights are here capitalized to create planar architected materials with a stretch-dominated response that can provide a large linear and rotational thermal expansion. What follows presents closed-form relations of their deformation (Δh, $\Delta\theta_1$) and CTE ($\alpha_{LCTE,y}$, α_{RCTE,θ_1}), along with a study that elucidates the role of temperature change.

3.1 Compound Units From Sub-Cells. Figure 4 illustrates the generation of compound units that use the primitive sub-cells (L and R) to generate large expansion. Therein are shown two sets of assembly rules used to create linear and rotational thermal expansion, respectively. In Fig. 4(a), reflection symmetry is first applied over the base of the L-sub-cell, and then translation along the periodic vectors parallel to the x and y axes of the coordinate system. The result is a pin-jointed tessellation of a bi-material lattice generated from a diamond-like linear unit (L-unit), which deforms of Δh (Eq. (7)) and has linear thermal expansion $\alpha_{LCTE,y}$ (Eq. (8)). On the other hand, Fig. 4(c) shows the generation of a lattice unit with rotational thermal expansion (R-unit). Here, two sequential symmetry operations applied to R-sub-cell yields a unit cell with rhomboidal shape, where four R-sub-cells share their high-CTE elements enclosed by a loop of low-CTE members. Upon a change in temperature, the bi-material lattice tilts at an angle $2\Delta\theta_1$, thus featuring a rotational CTE, described by the α_{RCTE,θ_1} of its primitive R-sub-cell, i.e., Eq. (6). While the metamaterial lattice concepts in Fig. 4 are constructed through specific operations onto sub-cell, the magnitude of deformation (i.e., Δh and $\Delta\theta_1$) and their CTE (i.e., $\alpha_{LCTE,y}$ and α_{RCTE,θ_1}) can be still described
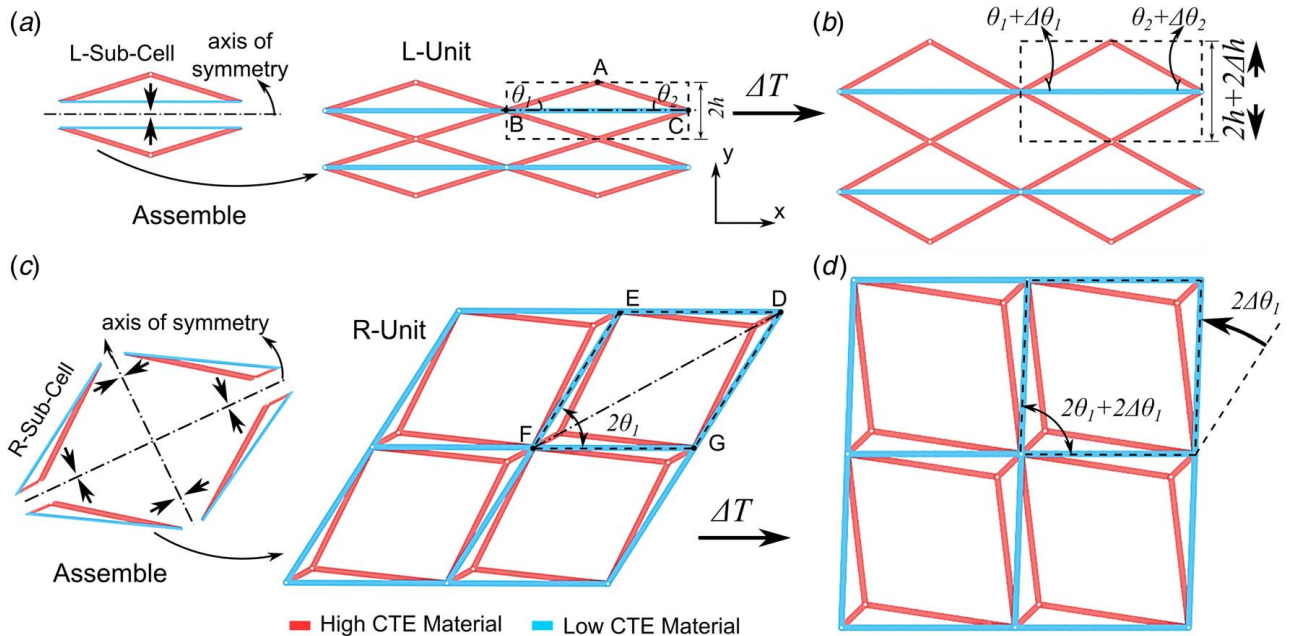

Fig. 4 Linear unit (L-unit) with linear CTE tunability in the undeformed (a) and deformed (b) state for given ΔT. Rotational unit (R-unit) with a rotational deformation and rotational CTE tunability in the undeformed (c) and deformed (d) states.

by those of their sub-cells, i.e., Eqs. (7), (8), (5), and (6), respectively.

3.2 The Role of Temperature Change. The results above pertain to responses accrued at a given representative ΔT. Here, we examine the effect of varying the temperature range on the deformation and CTE.

Figures 5(a) and 5(b) are plots of the linear and rotational deformation versus ΔT of our concepts. Both Δh and $\Delta \theta_1$ feature a monotonic increase, indicating the larger the temperature change, the greater the thermal deformation. This dependence, however, is not linear. Figures 5(a) and 5(b) reveal that through the range 0–100 °C, Δh and $\Delta \theta_1$ increase at a rate faster in the initial stage (e.g., ΔT from 0 °C to 20 °C) than in the final stage (e.g., ΔT from 80 °C to 100 °C). Hence, if maximizing deformation is sought for actuation, then ΔT can be selected accordingly unless it is imposed by the environment.

Analogous to Figs. 5(a) and 5(b), Figs. 5(c) and 5(d) show, respectively, the variation of LCTE and RCTE with ΔT. The highest value of CTE in both cases is for a folded triangle with sides resting on its base, and the overall trend is also here nonlinear. The impact on the CTEs, however, is antagonist to that on their respective deformations: the smaller the temperature change, the larger the CTE. The main reason stems from the CTE definition. For example for LCTE, Eq. (1) indicates that for a given h, a Δh increase in the numerator that is slower than the ΔT increase in the denominator can yield a sustained reduction in LCTE. For instance,

for a L-unit with $\theta_1 = \theta_2 = 2$ deg, a ΔT change from 2 °C to 100 °C decreases LCTE from 0.07 to 0.03, but the height of the unit cell (i.e., $h + \Delta h$) increases nonlinearly from 1.8 mm to 7 mm, four times of the initial height. Another role is that played by the skew angle on both CTEs (Figs. 5(c) and 5(d)). For example for LCTE, Fig. 5(c) shows that the trend of the L-unit with 2 deg is almost insensitive to ΔT as opposed to those with $\theta_1 = \theta_2 > 5$ deg. In summary, one important insight of this analysis is that a larger ΔT does increase Δh and $\Delta \theta_1$, but it also reduces LCTE and RCTE.

4 Thermal Expansion Amplification via Structural Hierarchy

Although structural hierarchy has been effective to achieve unbounded CTE tunability in bi-material lattices with rigid joints, yet the magnitude of the attainable deformation is not necessarily large [13]. For large-scale thermal deformation, the role of connection type becomes sizeable, and pin-joint connections in self-repeating lattices can fully exploit the amplitude of rotation that is cumulatively accrued at each level of the structural hierarchy. In this section, structural hierarchy is applied to pin-jointed lattices with the purpose of amplifying thermal deformation, other than CTE tunability. Here we provide closed-form expressions of the thermal expansion properties of hierarchical lattices, while present in Sec. 5 details on sample fabrication, CTE testing, and additional results from the computational analysis in Sec. 5.
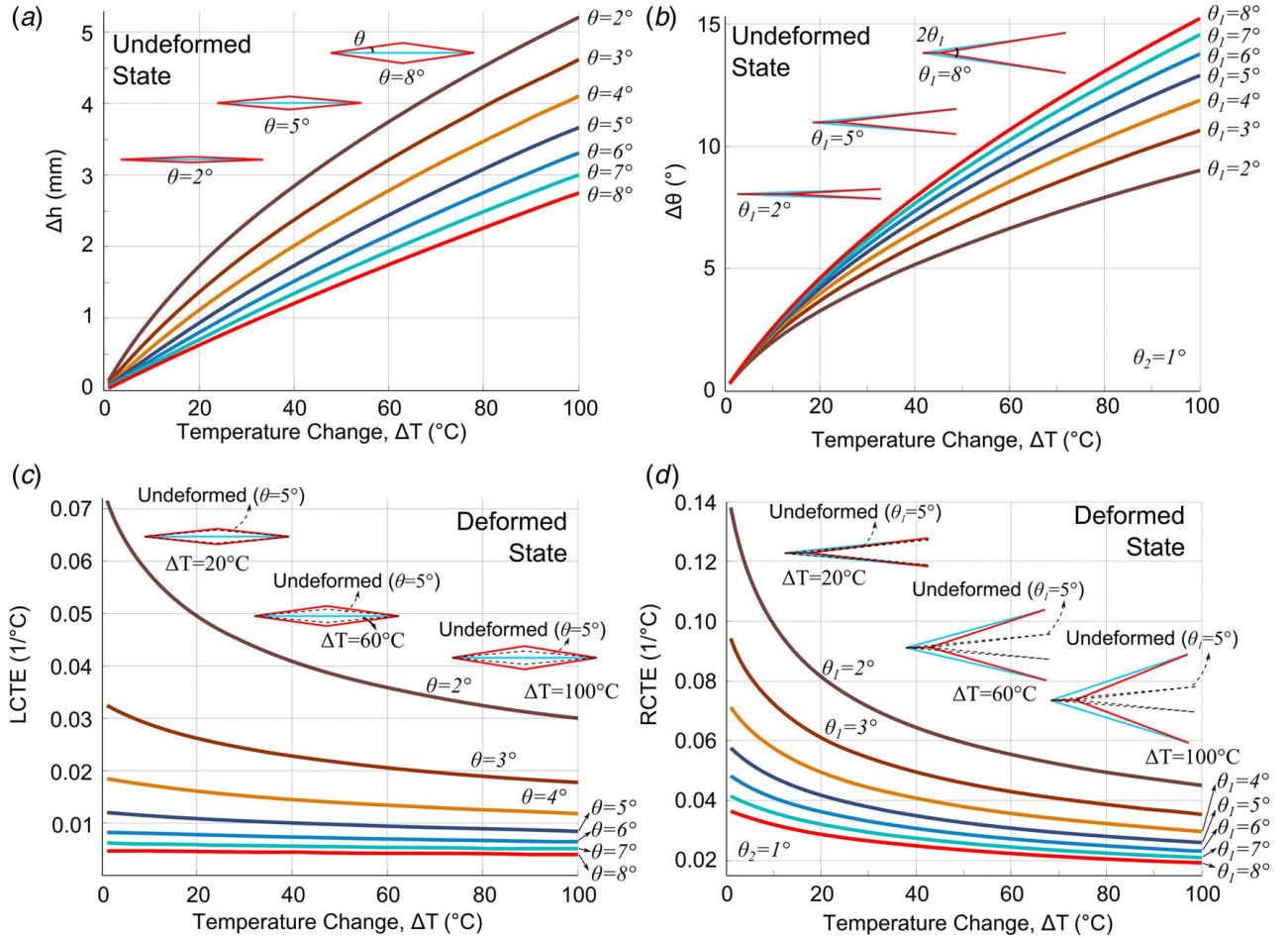

Fig. 5 Curves of (a) magnitude of the change in height Δh of L-unit, (b) magnitude of the change in the left skew angle, $\Delta \theta_1$, of R-unit, (c) LCTE of L-unit, and (d) RCTE of R-unit, versus temperature change ΔT parameterized by θ_1. Dash indicates undeformed configuration whereas continuous lines are used for the deformed state. Prescribed to all unit cells are $l_3 = 100$ mm, $\alpha_{s1} = 100 \times 10^{-6}$/°C, and $\alpha_{s2} = 10 \times 10^{-6}$/°C.

4.1 Temperature-Actuated Hierarchical Metamaterials.

As described in Sec. 2, the greater the CTE distinction of the constituent solids, i.e., high λ, the larger the effective coefficient of thermal expansion the L- and R-unit cells can offer with values above those of their constituent CTEs. We now create multiscale hierarchical lattice (HL) by replacing the high-CTE solid constituent with unit cells that have higher CTE values than those of their base materials [13]. By doing so, we can significantly boost the effective thermal expansion over that offered by their primitive units, i.e., L-unit and R-unit. This strategy is applied in Fig. 6, where hierarchical lattices are generated from the pin-jointed unit cells shown in Figs. 4(a) and 4(c). The advantage of using pin-joints over rigid connections becomes even more evident with HL, because the gain of deformation accumulates with the addition of each hierarchical order, hence contributing to the attainment of large thermal deformation.

Figures 6(a) and 6(b) show the undeformed and deformed L-unit under given ΔT. These correspond to the concepts with only one order of structural hierarchy (n = 1), and—as explained later in the fabrication section—their pin-joints are realized with flexural hinges. In Figs. 6(c) and 6(d), the concepts with n = 2 are shown in their original and deformed state. Similarly for the rotational deformation, Figs. 6(e) and 6(f) and Figs. 6(g) and 6(h) show the counterpart concepts with n = 1 and n = 2, respectively.

From a comparison of the L and R concepts (Fig. 6), we note that the former consists of self-repeating unit cells, i.e., a fractal-like lattice, while the latter combines the L-unit, taken as high-CTE component at n = 1, with the R-unit providing rotational deformation, at n = 2, hence creating a hybrid-type HL. For both concepts, however, all the elements in each order of the structural hierarchy are pin-jointed, a condition that enables large rotations at the shared lines or nodes. In addition, setting fabrication restrictions aside, we note that their degree of thermal expansion can be further enlarged by replacing the low-CTE solid with units offering lower CTE values than those of the base materials [13]; this path, however, is not pursued here.

For the analysis of temperature-actuated HL, we consider the general case of nth order HL of L and R type (L-HL and R-HL), respectively, with thermal expansion scale Δh_n and $\Delta \theta_{1,n}$, as well as effective CTEs $\alpha^*_{L,y,n}$ and $\alpha^*_{R,\theta_1,n}$. The high-CTE cell walls consist of L-units of effective CTE along the beam axial direction $\alpha^*_{L,y,n-1}$. The skew angle θ is given and common to all L concepts in all hierarchical orders, whereas the θ_1 and θ_2 are given for R-HL but only for the highest order, i.e., the order with rotational deformation. For both L-HL and R-HL, Δh_n and $\Delta \theta_{1,n}$ can be written as

$$\Delta h_n = l_{1,n}[(1 + \alpha^*_{L,y,n-1}\Delta T)^2 - \cos^2\theta(1 + \alpha_{s2}\Delta T)^2]^{1/2}$$
$$- l_{1,n} \sin \theta \quad \text{for L-HL} \tag{9}$$

$$\Delta \theta_{1,n} = \arccos\left(\frac{\xi_n^2 \sin(\theta_2 - \theta_1) + \sin(\theta_2 + \theta_1)}{2\xi_n \sin \theta_2}\right) - \theta_1 \quad \text{for R-HL} \tag{10}$$

where $\alpha_{L,y,0} = \alpha_{s1}$ and $\xi_n = (1 + \alpha^*_{L,y,n-1}\Delta T)/(1 + \alpha_{s2}\Delta T)$.

LCTE and RCTE for L-HL and R-HL with nth order of hierarchy can then be expressed as

$$\alpha^*_{L,y,n} = \frac{\sqrt{(1 + \alpha^*_{L,y,n-1}\Delta T)^2 - \cos^2\theta(1 + \alpha_{s2}\Delta T)^2}}{\Delta T \sin \theta} - \frac{1}{\Delta T} \quad \text{for L-HL} \tag{11}$$

$$\alpha^*_{R,\theta_1,n} = \left(\arccos\left(\frac{\xi_n^2 \sin(\theta_2 - \theta_1) + \sin(\theta_2 + \theta_1)}{2\xi_n \sin \theta_2}\right) - \theta_1\right) \Big/ (\theta_1 \Delta T)$$
$$\text{for R-HL} \tag{12}$$

4.2 Coefficient of Thermal Expansion Theoretical Predictions for Hierarchical Lattices.

Figure 7(a) is a plot of Eq. (11) illustrating the effective LCTE of L-HL with increasing hierarchical orders. Each of the lines represents LCTE values for a given skew angle θ starting from n = 0, solid materials, through n = 1, L-unit cell, followed by L-HL with increasing hierarchical order n = 2 and n = 3. The predictions provide discrete LCTE values, each obtained for given n, although the trends are shown as continuous to ease their interpretation within each figure. The first observation is the significant LCTE increase, especially at lower skew angles. For example, $\theta = 2$ deg with n = 3 provides over 4406 times more actuation performance than with n = 1. In addition, there is a large difference between pinned and rigid joint concepts, shown in black as a baseline in Fig. 7(a), and this distinction becomes more substantial at higher orders. For example, at $\theta = 8$ deg, for n = 1, the difference in the effective LCTE between concepts with pin and rigid joints is approximately 70.3%, whereas for n = 2, the value is roughly 177%. L-HLs with pin connections can thus offer large linear thermal expansion if low skew angles with high-hierarchical order are chosen, potentially achieving values rarely produced in the literature, e.g., beyond
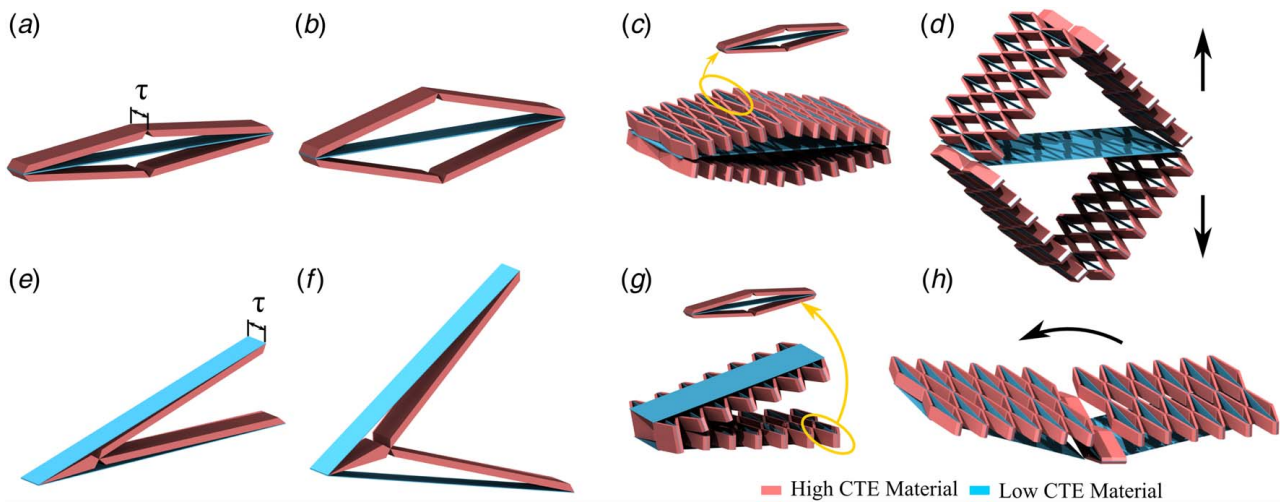

Fig. 6 Initial (a) and final (b) deformation modes of L-unit, initial (c) and final (d) deformation modes of L-HL (n = 2), initial (e) and final (f) deformation modes of R-unit, and initial (g) and final (h) deformation modes of R-HL (n = 2). τ is the out of the plane thickness of the concepts.
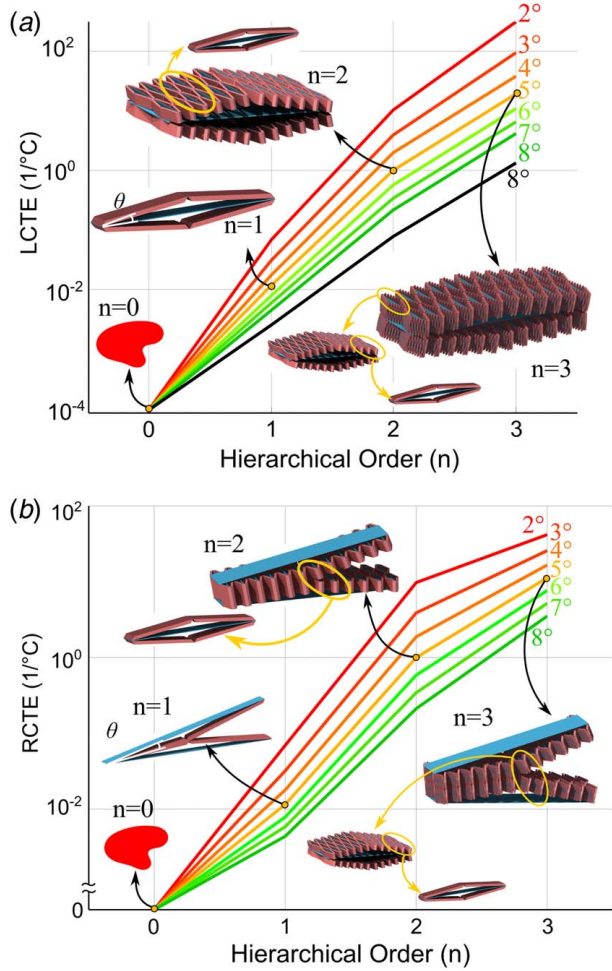
■ High CTE Material ■ Low CTE Material

Fig. 7 Semi-log plot of the LCTE in the *y*-direction (*a*) and RCTE of θ_1 (*b*) of hierarchical lattices versus the number of hierarchical orders n for given skew angle $\theta = \theta_1 = \theta_2$ with an integer $\theta \in [2 \text{ deg}, 8 \text{ deg}]$, $\alpha_{s1} = 100 \times 10^{-6}/°C$, $\alpha_{s2} = 10 \times 10^{-6}/°C$, and $\Delta T = 1 °C$. LCTE of L-HL with rigid joints is shown as a baseline in black in (*a*).

100% strains typically achieved by electroactive polymers for identical temperature range [23].

Similarly to LCTE, the RCTE is shown in Fig. 7(*b*) for R-HL as a function of hierarchical order. All plotted lines are obtained from Eq. (12) with a representative pair of equal skew angles $\theta_1 = \theta_2$, starting from n = 0, solid materials with $\alpha_{R,\theta_1,n=0} = 0$. Here, we observe that as the order increases from 0 to 1, the effective RCTEs become nonzero showing rotational thermal deformation. As the order changes from 1 to 2, RCTEs increase more drastically and larger once more from order 2 to 3. Taking $\theta_1 \approx 8$ deg, as an example, the RCTE of R-HLs enlarges from $\alpha_{R,\theta_1,n=1} = 0.00458/°C$ to $\alpha_{R,\theta_1,n=2} = 0.213/°C$, and for n = 3, with only $\Delta T = 1 °C$, the R-HL provides an angle change of 35.5 deg, 4.45 times of its initial value. Be akin to LCTE, RCTE increases with the order of hierarchy, so as to approach a theoretically unbounded value for unlimited n and to obtain sizeable rotational actuation.

5 Sample Fabrication and Experimental Validation

Two sets of fabricated proofs-of-concept with first and second hierarchical order were experimentally tested in a heating chamber, and a set of numeric analyses of models with geometries matching those of the physical prototypes was also conducted to validate the theoretical predictions.

Table 1 Material properties of solid constituents for proof-of-concept prototypes

Material	CTE (×10⁻⁶/°C)	Young's modulus (GPa)	Poisson's ratio	Density (Kg/m³)
Delrin®	104 (−40 to 29 °C); 122 (29 to 60 °C); 137 (60 to 104 °C); 149 (104 to 149 °C)	3.1	0.35	1420
Steel	14.7 (20 to 700 °C)	210	0.3	7870

5.1 Fabrication of Proofs-of-Concept. A representative pair of materials (1080 Spring Steel chosen as the low-CTE material, and Delrin®, an acetal resin, as the high-CTE material) was chosen to fabricate proof-of-concept prototypes, although other pairs of solids, such as Al6061 and Ti-6Al-4 V, could also be selected. Table 1 provides their mechanical properties with temperature-dependent CTEs used in our analysis.

The manufacture of prototypes consisted of a combination of laser cutting and part assembling. In the first step (Fig. 8(*a*)), sheets of 1.59 mm thickness of Delrin® were laser cut (TROTEC Laser GmbH, Austria) to build cell walls with their corresponding flexure joints. Our laser cutter was first calibrated to provide planar deviations within ±0.05 mm. In the second step, through-holes with 0.75 mm diameter were drilled on two extremities of each sub-cell via a milling machine (Fig. 8(*b*)). Steel wires with 60 mm length and 0.5 mm diameter were then individually embedded to the drilled through-holes, and epoxy glue (Gel Epoxy Syringe Glue, LePage) was applied to provide adherence between materials (Fig. 8(*c*), step 3).

As per the joint realization, Figs. 8(*d*I) and 8(*d*II) show the adoption of notch joints [24] in the first-order sub-cells to enable rotation at the connections. These local notches act as living hinges with much lower bending stiffness than those offered by beam elements with un-notched section, thus enabling node rotation (Figs. 8(*d*III) and 8(*d*IV)). Different from the first-order sub-cells, hinges in the second-order hierarchical configuration consist of ring bolts (Fig. 8(*e*)) of 1.59 mm thickness, which were laser cut and bonded to the extremities of the second-order beam elements via epoxy glue. At the second order, the hinges are assumed to be perfect pins insensitive to friction or wear. As a result, second-order beam elements can rotate freely.

The experimental procedure consisted of testing the thermal deformation of samples placed in a heating chamber with temperature monitored and managed through a proportion-integration-differentiation controller (CN7800; Omega, Norwalk, CT). A 3D digital image correlation (DIC) system was used for thermally responsive samples with spatial deformation. The effective thermal deformations were calculated by measuring the change in distance between member connections. In total, two sets of DIC experiments were undertaken for a total of four tests, two for each set with multiple measures taken. In the first group (Fig. 9), DIC was applied to an L-unit cell (Fig. 9(*a*)) and a half-reduced R-unit cell (Fig. 9(*b*)) with one order of hierarchy. Both units have given a length of 56 mm with the thickness of each beam element of 1.6 mm, a value much larger than the 0.2 mm thickness of the notch joints. Relying on their compliance, these slender notch joints can produce the desired degree of rotation. With the aim of obtaining large thermal deformation, a shallow skew angle of $\theta = 2.65$ deg was selected for the L concept, and $\theta_1 = 9.00$ deg and $\theta_2 = 1.18$ deg for the R concept.

The second set of results in Figs. 10(*a*) and 10(*c*) features DIC data for second order samples. L-unit with all dimensions identical to those of the first set (Fig. 9(*a*)) were selected to replace the high-CTE solid component of L and R concepts, thus forming the second-order proof-of-concept. As shown in Figs. 10(*a*) and 10(*c*), along the length direction of the second-order beam elements, there
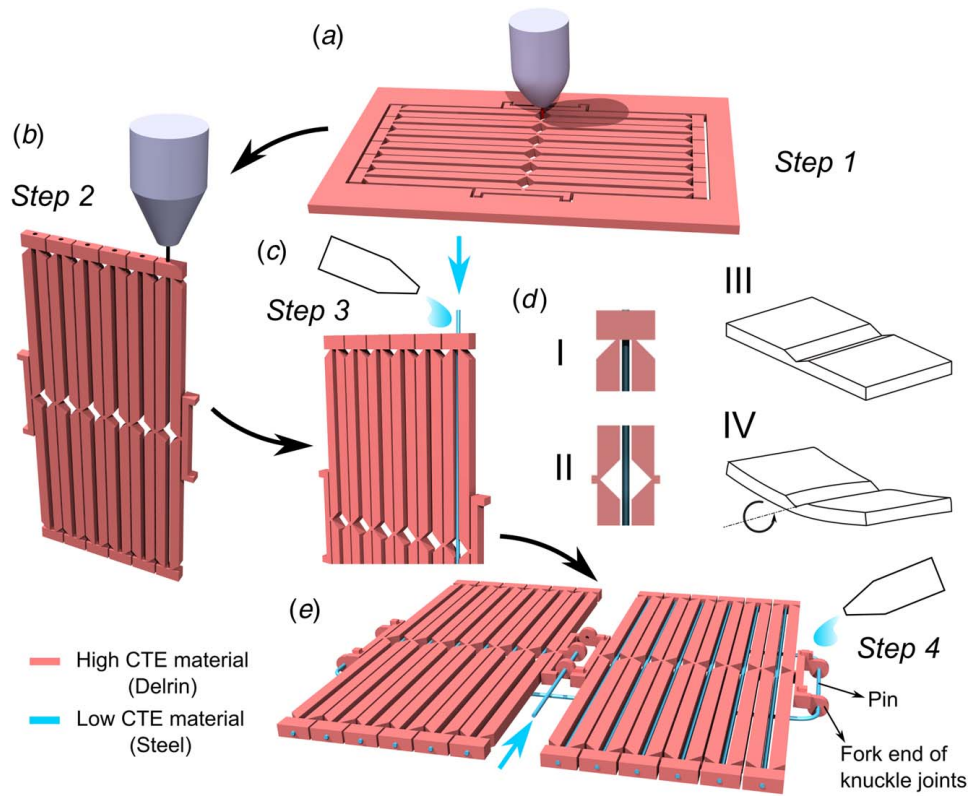
Fig. 8 Fabrication process of proofs-of-concept: (*a*) laser cutting, (*b*) drilling via milling machine, (*c*) insertion and fixation of steel wires, (*d*) notch joints of a L-unit (I and II) as well as sketches of notch joints before (III) and after (IV) thermal deformation, and (*e*) fixation of flakes with fork end of knuckle joints and assembly of hierarchical proof-of-concepts
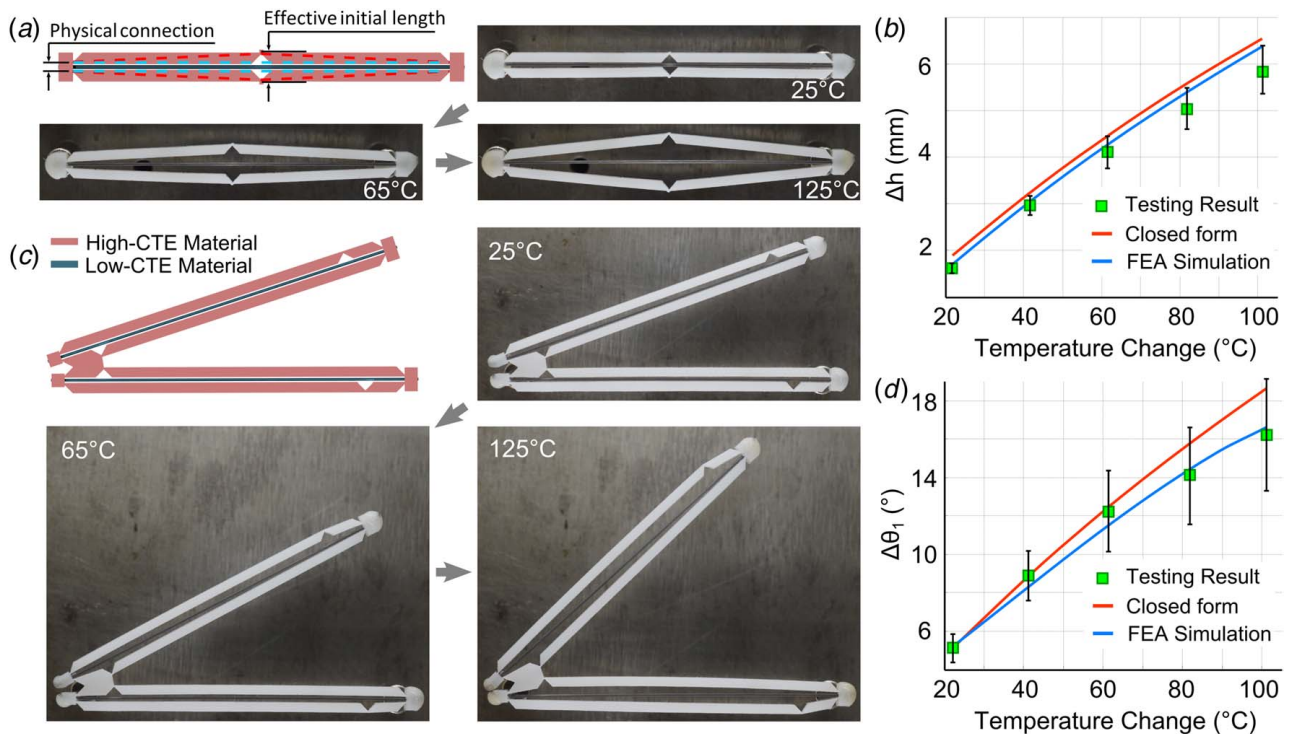

Fig. 9 Schematics of the first-order L-unit cell (*a*) and R-unit cell (c) with their initial configuration, fabricated sample, and thermal deformation. (*b*) and (*d*) The values of Δh and $\Delta\theta_1$ experimentally observed, computationally determined, and theoretically obtained.
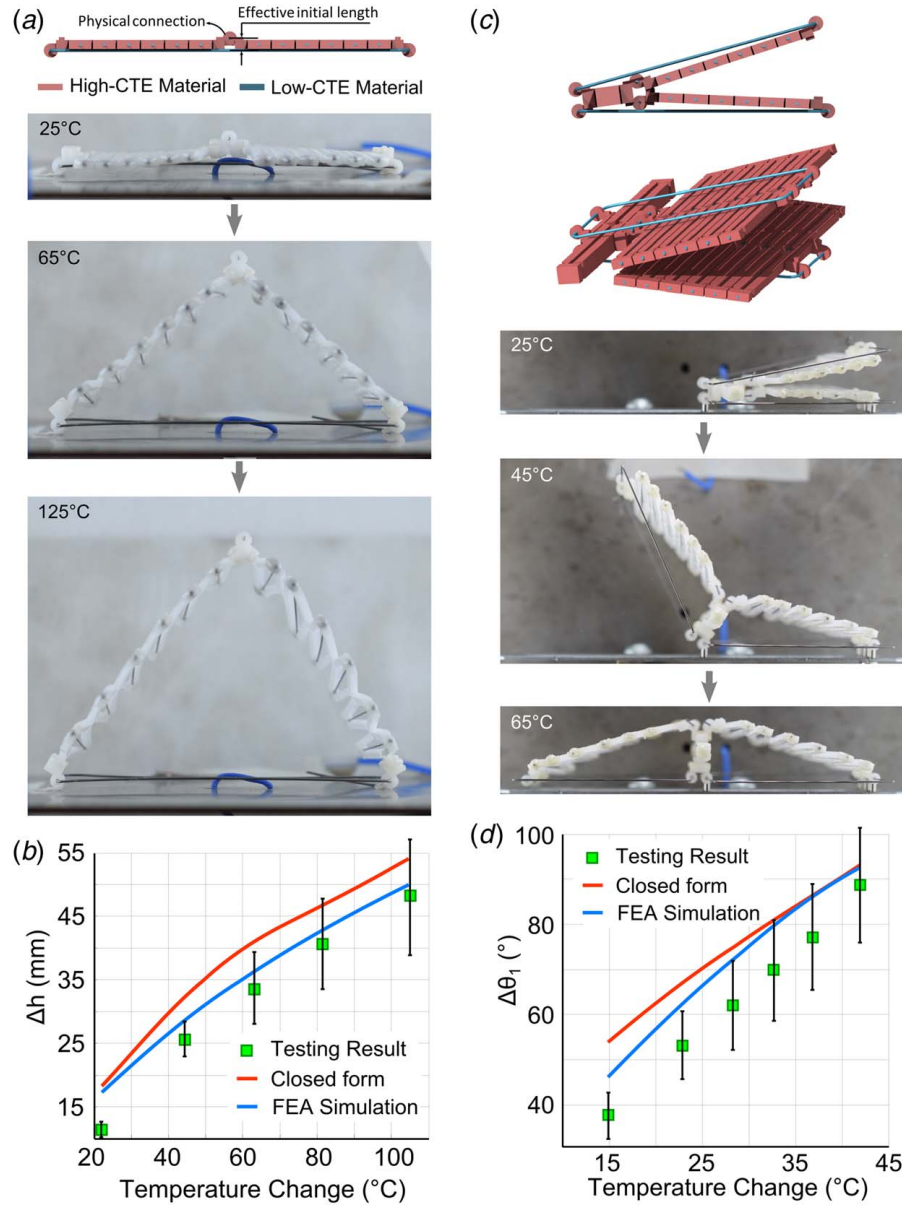
Fig. 10 Schematic of the second-order L-HL (a) and R-HL (c), each with their initial config-
uration, fabricated sample, and thermal deformation. (b) and (d) show values of $\Delta h_{n=2}$
and $\Delta\theta_{1,n=2}$ experimentally observed, computationally calculated, and obtained through
closed-form expressions.

are six L-units on the skew sides of the L sample and on the side opposite of θ_1 for the R sample. The side opposite of θ_2, however, is constructed by one L-unit only. A skew angle of $\theta = 9.25$ deg was chosen for the L-HL concept, while $\theta_1 = 9.80$ deg and $\theta_2 = 3.55$ deg for the R-HL samples. In all tests, $\Delta T = 100\,°C$ (from 25 °C to 125 °C) was chosen except for the test of the second-order R hierarchical sample, where $\Delta T = 40\,°C$ (from 25 °C to 65 °C) because this sample attained a very large deformation (beyond π rad).

5.2 Results From Experiments, Theory, and Computations. Figures 9 and 10 show first- and second-order proofs-of-concept along with their linear (sub-figure *a*) and rotational (sub-figure *c*) thermal deformation. In particular, sub-figures *b* and *d* in Figs. 9 and 10 show their CTE values obtained from testing, closed-form predictions, and computational analysis. Below, we first describe the overall actuation performance and

then explain the deviations between the three sets of results therein included.

Figures 9(*a*) and 9(*b*) illustrate that the L concept (n = 1 with $\theta = 2.65\,°C$) without structural hierarchy can increase the LCTE along the *y*-direction from $149 \times 10^{-6}/°C$ (n = 0, i.e., the high-CTE component material, Delrin®) to $13{,}009 \times 10^{-6}/°C$, about 86 times higher than the CTE of (α_{s1}) component. For increasing hierarchical order, L-HL (Fig. 10(*a*), n = 2 with $\theta = 9.25$ deg) can further boost the effective LCTE in the *y*-direction to $79{,}422 \times 10^{-6}/°C$, 532 times higher than α_{s1}. By adding hierarchical orders from n = 1 to n = 2, the L concept shows an LCTE increase up to 6.1 times. With respect to the linear displacement, for a temperature change of 100 °C, the L concept with n = 1 expands its height from 4.4 mm to 10.2 mm, while with n = 2, this expansion is from 5.8 mm to 51.5 mm, i.e., almost nine times of the initial height.

Figures 9(*c*) and 9(*d*) illustrate that the R concept (n = 1 with $\theta_1 = 9.00$ deg and $\theta_2 = 1.18$ deg) can offer a very pronounced rotational deformation with RCTE of $18{,}341 \times 10^{-6}/°C$. With a higher order
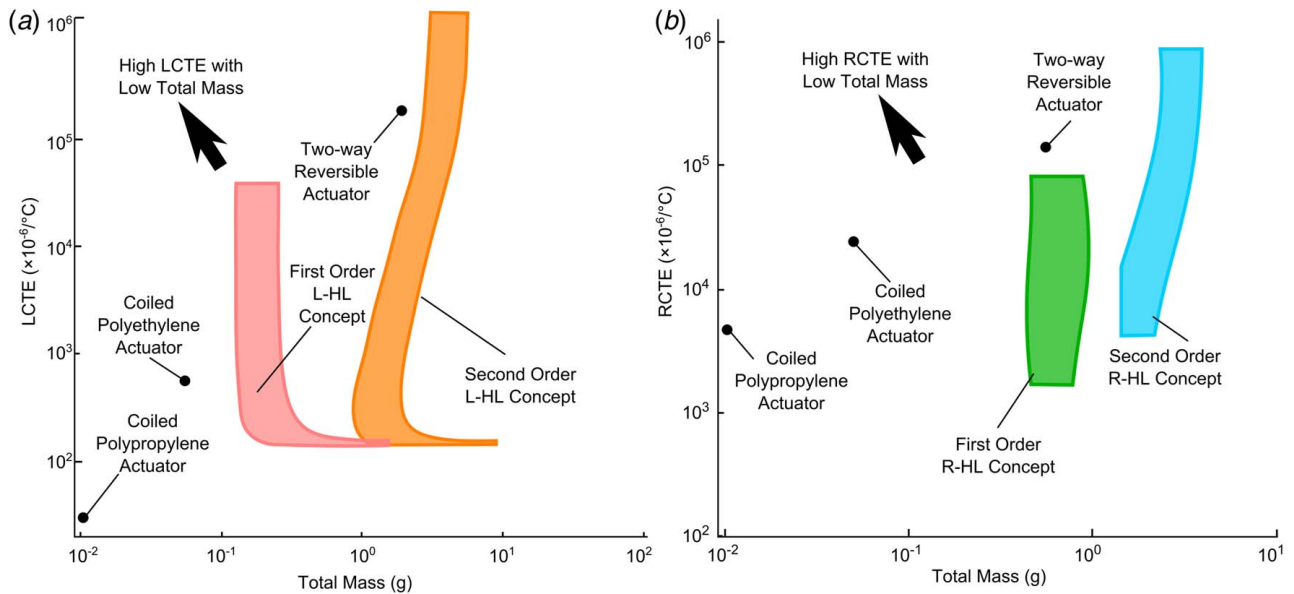
Fig. 11 Representative thermally actuated mechanisms [8,25] along with (a) LCTE of L concept and (b) RCTE of R concept for increasing hierarchical order (from n = 1 to n = 2) plotted against total mass. Delrin® and steel are chosen as base materials. All subcells have beam element length (Fig. 1) $l_3 = 50$ mm and out of plane thickness (Fig. 6) $\tau_{n=1} = 1$ mm and $\tau_{n=2} = 50$ mm.

of structural hierarchy, the R concept (Fig. 10(c), n = 2 with $\theta_1 =$ 9.80 deg and $\theta_2 = 3.55$ deg) can further increase the effective RCTE to $432,231 \times 10^{-6}/°C$, almost 23 times higher than the concept with n = 1. As per the scale of the rotational deformation, for $\Delta T = 100\,°C$, the first-order R concept expands the initial angle from $\theta_1 = 9.00$ deg to 25.50 deg, while the second-order needs only a $\Delta T = 40\,°C$ to increase θ_1 from 9.80 deg to 179.23 deg, nearly rotating by 180 deg.

To explain the reasons for the deviation between the three sets of results (experiments, theory, and computations), we first describe the conditions under which the results were obtained. For all the analyses, the properties used for the constituent materials were those in Table 1 with values varying with temperature. In the theoretical analysis, nodes were considered as ideal pins that allow free rotation, whereas flexure hinges were implemented in the 3D computational models with geometries matching those of the physical prototypes (Fig. 9). In the computational analysis, nonlinear finite element analyses (FEA) were performed via ANSYS 14.5 (ANSYS Inc., Canonsburg, PA), and all models were meshed using 20-node hexahedral elements and simulated under given temperature changes. For the first-order concepts, flexural hinges (Fig. 9) were modeled, and for the second-order concepts, ideal hinges were allowed to rotate freely (Fig. 10).

Given the description above, several reasons can be identified to explain the deviations between experimental, theoretical, and computational results shown in sub-figures b and d of Figs. 9 and 10. The discrepancy between theory and computations can be attributed to the adoption of ideal pins (theory) versus flexural hinges (FEA). On the other hand, the difference between computational and experimental results is mainly caused by three factors: manufacturing defects, such as dimensional deviations introduced during laser cutting, friction between the testing plate and the samples, as well as complications in maintaining a uniform temperature in the heating chamber. As per the magnitude of deviations between results in Figs. 9(b) and 9(d), the error between testing results and closed-form predictions is within 10% considering the ultimate thermal deformation, i.e., the deformation calculated at the upper limit of a given temperature range, of each test, and the difference between testing and computational values only go as high as 8.9%. As per the deviations reported in Figs. 10(b) and 10(d), we note that during the initial stages of deformation, the error between experimental data and theoretical results can reach 30%.

The main cause can be attributed to tolerances existing between the pin and the fork end of knuckle joints (Fig. 8(e)). In a regime characterized by small temperature changes, the thermal expansion of beam elements first offsets any tolerances existing between parts, and only later, once existing gaps are closed, the actual expansion takes place.

The error bars in sub-figures b and d of Figs. 9 and 10 show the standard deviation (SD) of multiple tests. As described, SDs can be mainly attributed to the testing apparatus, i.e., friction between testing plate and specimen, the variation of the average temperature measured during each test by the four thermocouples located in the heating chamber and manufacturing accuracy, which yields defects of slightly dissimilar amplitude during fabrication. Furthermore, compared with those of the first order, the SDs of the second-order are larger, because defects accumulate with hierarchical order.

Discussion

The stretch-dominated sub-cells and their hierarchical implementations can be considered as programmable truss-like materials that can yet attain large linear and rotational deformation in response to a temperature change. Because in certain applications, such as in aerospace, the need for large actuation is often coupled with the requirement of low mass, in this section we discuss and compare their CTE performance and mass potential with a set of representative thermal actuators including coiled polyethylene and polypropylene actuators as well as a two-way reversible actuator [8,25].

Figure 11 shows plots of LCTE and RCTE (Eqs. (11) and (12)) versus total mass (derivation in the Appendix) with the top left indicating high CTE and low total mass. The data populate regions of the material and geometric space featuring a distinct scale of tailorable linear (Fig. 11(a)) and rotational (Fig. 11(b)) thermal expansion. For L concepts with given $l_3 = 50$ mm and $\Delta T = 100\,°C$, two domains (Fig. 11(a)) describing the change of LCTE with total mass for n = 1 concepts and for n = 2 emerge from a parametric study of the unit cell, where the initial skew angle $\theta \in [1\deg, 89\deg]$ and the bar thickness ratio $t/l_3 \in$ [0.004, 0.02] are the active variables for a given pair of materials (i.e., Delrin® and Steel with properties in Table 1). Similarly for the rotational thermal expansion, Fig. 11(b) shows two

domains, the left for $n = 1$ and the right for $n = 2$, both obtained via a parametric study of the unit cell with active variables: $\theta_1 \in [2 \deg, 45 \deg]$, $\theta_1 \in [1 \deg, 22 \deg]$, and $t/l_3 \in [0.004, 0.02]$ for both $n = 1$ and $n = 2$.

Overall for all the concepts, the trade-offs shown in Fig. 11 between the two properties corroborate that an attempt of increasing CTEs results in an increase of total mass. L-HL concepts with $n = 2$ have higher total mass than those with $n = 1$, yet their LCTE can range from nearly that of the high-CTE base material, i.e., Delrin®, to more than $10^6 \times 10^{-6}/°C$, three orders of magnitude higher. Similarly, at the cost of total mass, RCTE for $n = 1$ can be further amplified via an additional hierarchical order. On the other hand, coiled polyethylene and polypropylene actuators have much lower total mass than HL concepts, but the maximum L- and RCTEs they can offer are two to three orders of magnitude smaller than that of L- and R-HLs. This sets certain limitations in engineering applications demanding large thermal deformation. In contrast, the thermally actuated two-way reversible actuator provides two sizeable CTE values that are comparable with HL concepts. The HL concepts, however, provide a larger number of trade-offs to select from with values obtained via architecture tuning. The lightweight and CTE performance of the stretch-dominated sub-cells and their hierarchical implementations here presented can thus be considered as lightweight candidates for applications requiring large linear and rotational thermal actuation.

While the concepts presented in this work show promises for planar actuation, extensions to 3D for spatial actuation are feasible, and fabrication via other processes, such as 3D printing, is possible. Their potential, however, should always be confronted with the capabilities of current practices of fabrication. The concepts are in principle scale independent and material selection free, yet increasing the order of structural hierarchy has to account for the limits imposed by a given manufacturing process [26].

Conclusions

The focus of this work has been on temperature-induced actuation that bi-material triangular units can offer for not only linear but also rotational deformation and coefficient of thermal expansion. We have shown that structural hierarchy can be effective in enlarging the magnitude of thermal expansion while guaranteeing low mass levels. Through experiments, theoretical expressions and simulations on fabricated proof-of-concepts, our results have shown that concepts with second-order hierarchy can provide linear thermal displacement of 8.9 times the initial height and rotational displacement of 18.3 times the initial skew angle. These large-scale values of thermal actuation achieved via the addition of only one order of hierarchy are up to 6.1 times (for L with $\Delta T = 100\,°C$) and 19 times (for R with $\Delta T = 40\,°C$) higher than what can be obtained through unit cells in the first order. The class of architected materials here presented takes one step closer to meeting the demands of thermally functional materials that are stiff and lightweight and can be engineered to provide customized levels of thermal deformation for next-generation actuators, deployable space systems, MEMS, and biomedical sensors.

Appendix

To generate the regions in Fig. 11, we used the expressions of the total mass M of the concepts that we experimentally tested. For L- and R-sub-cells with arbitrary skew angles (Fig. 4), the total mass is given by

$$M_{\text{L-Unit},n1} = t\tau(4l_1\rho_{\text{Delrin}} + l_3\rho_{\text{Steel}}) \quad \text{for L-unit} \qquad (A1)$$

$$M_{\text{R-Unit},n1} = t\tau(2l_1\rho_{\text{Delrin}} + 4l_2\rho_{\text{Delrin}} + 2l_3\rho_{\text{Steel}}) \quad \text{for R-unit}$$
$$(A2)$$

where t is the strut thickness, τ is the out of plane thickness, l_1, l_2, and l_3 are bar lengths (Fig. 1), and ρ is the density of solid constituent (Table 1).

For HL with $n = 2$, the total mass for L-HL and R-HL are, respectively, given by

$$M_{\text{L-Unit},n2} = t_{n=2}\tau_{n=2}\left[2\left(\frac{l_{1,n=2}}{h_{n=1}}\right)M_{\text{L-Unit},n1} + l_{3,n=2}\rho_{\text{Steel}}\right] \quad \text{for L-HL}$$
$$(A3)$$

$$M_{\text{R-Unit},n2} = t_{n=2}\tau_{n=2}$$
$$\left[\left(\frac{l_{1,n=2}}{h_{n=1}}\right)M_{\text{L-Unit},n1} + 2\left(\frac{l_{1,n=2}}{h_{n=1}}\right)M_{\text{L-Unit},n1} + 2l_{3,n=2}\rho_{\text{Steel}}\right] \quad \text{for R-HL}$$
$$(A4)$$

where $h_{n=1}$ is the height of the sub-cell shown in Fig. 1, and $\tau_{n=1}$ and $\tau_{n=2}$ are the out of plane thickness at a given hierarchical order n.

References

[1] Ding, Z., Yuan, C., Peng, X., Wang, T., Qi, H. J., and Dunn, M. L., 2017, "Direct 4D Printing Via Active Composite Materials," Sci. Adv., **3**(4), p. e1602890.

[2] Ge, Q., Sakhaei, A. H., Lee, H., Dunn, C. K., Fang, N. X., and Dunn, M. L., 2016, "Multimaterial 4D Printing With Tailorable Shape Memory Polymers," Sci. Rep., **6**, p. 31110.

[3] Boatti, E., Vasios, N., and Bertoldi, K., 2017, "Origami Metamaterials for Tunable Thermal Expansion," Adv. Mater., **29**(26), pp. 1700360.

[4] Zhang, Q., Wommer, J., O'Rourke, C., Teitelman, J., Tang, Y., Robison, J., Lin, G., and Yin, J., 2017, "Origami and Kirigami Inspired Self-Folding for Programming Three-Dimensional Shape Shifting of Polymer Sheets With Light," Extreme Mech. Lett., **11**(Suppl. C), pp. 111–120.

[5] Breger, J. C., Yoon, C., Xiao, R., Kwag, H. R., Wang, M. O., Fisher, J. P., Nguyen, T. D., and Gracias, D. H., 2015, "Self-Folding Thermo-Magnetically Responsive Soft Microgrippers," ACS Appl. Mater. Interfaces, **7**(5), pp. 3398–3405.

[6] Stoychev, G., Puretskiy, N., and Ionov, L., 2011, "Self-Folding All-Polymer Thermoresponsive Microcapsules," Soft Matter, **7**(7), pp. 3277–3279.

[7] Yong, Z., and Tzu-Hsuan, C., 2015, "A Review of Microelectromechanical Systems for Nanoscale Mechanical Characterization," J. Micromech. Microeng., **25**(9), p. 093001.

[8] Mao, Y., Ding, Z., Yuan, C., Ai, S., Isakov, M., Wu, J., Wang, T., Dunn, M. L., and Qi, H. J., 2016, "3D Printed Reversible Shape Changing Components With Stimuli Responsive Materials," Sci. Rep., **6**, p. 24761.

[9] Wei, K., Peng, Y., Wang, K., Duan, S., Yang, X., and Wen, W., 2018, "Three Dimensional Lightweight Lattice Structures With Large Positive, Zero and Negative Thermal Expansion," Compos. Struct., **188**, pp. 287–296.

[10] Hopkins, J. B., Lange, K. J., and Spadaccini, C. M., 2013, "Designing Microstructural Architectures With Thermally Actuated Properties Using Freedom, Actuation, and Constraint Topologies," ASME J. Mech. Design, **135**(6), p. 061004.

[11] Wang, Q., Jackson, J. A., Ge, Q., Hopkins, J. B., Spadaccini, C. M., and Fang, N. X., 2016, "Lightweight Mechanical Metamaterials With Tunable Negative Thermal Expansion," Phys. Rev. Lett., **117**(17), p. 175901.

[12] Steeves, C. A., Maxwell, P. T., He, M., and Evans, A. G., 2007, "Design of a Robust, Multifunctional Thermal Protection System Incorporating Zero Expansion Lattices," Proceedings of the ASME 2007 International Mechanical Engineering Congress and Exposition, Seattle, WA, Nov. 11–15, pp. 255–260.

[13] Xu, H., Farag, A., and Pasini, D., 2017, "Multilevel Hierarchy in Bi-Material Lattices With High Specific Stiffness and Unbounded Thermal Expansion," Acta. Mater., **134**, pp. 155–166.

[14] Steeves, C. A., dos Santos e Lucato, S. L., He, M., Antinucci, E., Hutchinson, J. W., and Evans, A. G., 2007, "Concepts for Structurally Robust Materials That Combine Low Thermal Expansion With High Stiffness," J. Mech. Phys. Solids, **55**(9), pp. 1803–1822.

[15] Lehman, J., and Lakes, R. S., 2014, "Stiff, Strong, Zero Thermal Expansion Lattices Via Material Hierarchy," Compos. Struct., **107**, pp. 654–663.

[16] Wei, K., Chen, H., Pei, Y., and Fang, D., 2016, "Planar Lattices With Tailorable Coefficient of Thermal Expansion and High Stiffness Based on Dual-Material Triangle Unit," J. Mech. Phys. Solids, **86**, pp. 173–191.

[17] Lakes, R., 1996, "Cellular Solid Structures With Unbounded Thermal Expansion," J. Mater. Sci. Lett., **15**(6), pp. 475–477.

[18] Xu, H., Farag, A., and Pasini, D., 2018, "Routes to Program Thermal Expansion in Three-Dimensional Lattice Metamaterials Built From Tetrahedral Building Blocks," J. Mech. Phys. Solids, **117**, pp. 54–87.

[19] Nye, J. F., 1985, *Physical Properties of Crystals: Their Representation by Tensors and Matrices*, Clarendon Press, Oxford

[20] Santiago-Prowald, J., and Baier, H., 2013, "Advances in Deployable Structures and Surfaces for Large Apertures in Space," CEAS Space J., **5**(3), pp. 89–115.

[21] Uchino, K., 1998, "Materials Issues in Design and Performance of Piezoelectric Actuators: an Overview," Acta Mater., **46**(11), pp. 3745–3753.

[22] Van Humbeeck, J., 1999, "Non-medical Applications of Shape Memory Alloys," Mater. Sci. Eng. A, **273**, pp. 134–148.

[23] Bar-Cohen, Y., 2004, *Electroactive Polymer (EAP) Actuators as Artificial Muscles : Reality, Potential, and Challenges*, SPIE Press, Bellingham, WA.

[24] Howell, L. L., 2001, *Compliant Mechanisms*, Wiley, New York.

[25] Aziz, S., Naficy, S., Foroughi, J., Brown, H. R., and Spinks, G. M., 2017, "Effect of Anisotropic Thermal Expansion on the Torsional Actuation of Twist Oriented Polymer Fibres," Polymer, **129**, pp. 127–134.

[26] Zheng, X., Smith, W., Jackson, J., Moran, B., Cui, H., Chen, D., Ye, J., Fang, N., Rodriguez, N., Weisgraber, T., and Spadaccini, C. M., 2016, "Multiscale Metallic Metamaterials," Nat. Mater., **15**(10), pp. 1100–1106.